Physica D ▮ (▮▮▮▮) ▮▮▮–▮▮▮

Contents lists available at ScienceDirect

Physica D

journal homepage: www.elsevier.com/locate/physd

Shape oscillations of a droplet in an Oldroyd-B fluid

J.C. Chrispell [a,c,*], R. Cortez [a,c], D.B. Khismatullin [b,c], L.J. Fauci [a,c]

[a] Department of Mathematics, Tulane University, New Orleans, LA 70118, USA
[b] Department of Biomedical Engineering, Tulane University, New Orleans, LA 70118, USA
[c] Center for Computational Science, Tulane University, New Orleans, LA 70118, USA

ARTICLE INFO

Article history:
Available online xxxx

Keywords:
Immersed boundary
Oldroyd-B
Viscoelastic droplet

ABSTRACT

We present a Navier–Stokes/Oldroyd-B immersed boundary algorithm that captures the interaction of a flexible structure with a viscoelastic fluid. In particular, we study the effects of bulk viscoelasticity on freely decaying shape oscillations of an Oldroyd-B fluid droplet suspended in an Oldroyd-B matrix. Our numerical data indicate that if the fluid viscosity is low, viscoelasticity plays a modulating role in the drop shape relaxation; specifically, it increases the oscillation frequency and decreases the decay rate when the fluid relaxation time is above a critical value. In the high viscosity limit, i.e., when a Newtonian droplet is expected to return to a spherical shape with an aperiodic decay, an increase in the relaxation time eventually results in the reappearance of the oscillations. Both these results are in line with the prediction of small deformation theory for viscoelastic droplet oscillations. The algorithm was also validated by direct comparison with linear asymptotics.

1. Introduction

An incompressible liquid droplet with surface tension is one of the classical models in hydrodynamics. It plays an important role in the description of various physical and biological systems such as emulsions and foams [1–3], fogs and clouds [4,5], molten metals [6,7], the Earth and other astrophysical objects [8–10], atomic nuclei [11,12], and living cells [13–15]. In the absence of external forces, droplet dynamics are determined by surface tension and bulk rheological properties of the fluids inside and outside the droplet. Surface tension is responsible for a spherical shape of the droplet at equilibrium and is also an important factor in the droplet shape relaxation [16]. After removal of external forces, a Newtonian liquid droplet of low shear viscosity returns to its equilibrium shape via a series of underdamped oscillations with frequency and damping rate dependent on the surface tension and shear viscosity, respectively [17]. The droplet shape oscillations cease to exist, i.e., only an aperiodic decay is observed, when the viscosity of the internal liquid exceeds a critical value [9]. The critical viscosity is a function of the normal mode of shape oscillations. For the principal mode ($n = 2$, i.e., quadrupole oscillation) of a 0.1 mm radius droplet suspended in air, it is about 0.0655 Pa s [18,9]. The critical value of the shear viscosity decreases quadratically with decrease in the droplet radius [9]. Since the internal viscosity of living cells is several magnitudes higher than 0.0655 Pa s and the cell radius is less than 0.1 mm, this result indicates that the Newtonian model of a living cell will always predict cell shape relaxation via an aperiodic decay.

Several numerical methods have successfully simulated nonlinear oscillations of Newtonian liquid droplets. This includes boundary integral [19,20], boundary element [21], and finite element methods [22] as well as surface capturing techniques such as volume-of-fluid and level set methods [23]. Moreover, the coupling of the flexible boundary of a droplet to an enclosed and surrounding incompressible fluid has been a standard model problem in the development and analysis of immersed boundary methods. It has been used as a test problem for the development of higher order algorithms [24], implicit implementations [25,26], and most recently in a proposed model of porous immersed boundaries [27].

Living cells and many other droplet-like systems do not behave, however, as Newtonian liquid droplets because of the bulk elasticity of their fluids. For eukaryotic cells, the elasticity of the internal liquid comes from the cytoskeleton. Prokaryotic microorganisms such as bacteria are often suspended in viscoelastic fluids, e.g., when they move in the cell cytoplasm or through a mucosal layer of a specific organ. The dynamics of these systems will be correctly described only if viscoelastic effects are accounted for. In addition, understanding the effects of bulk and surface viscoelasticity on droplet shape relaxation is of paramount importance for the development of advanced methods for rheological measurement of fluids [18,28,29]. While the oscillatory dynamics of liquid droplets with a viscoelastic surface layer is well studied in the literature [30,31,29,32–34], there are only a few reports concerning shape oscillations of viscoelastic liquid droplets [18,35,36]. Most are based

* Corresponding author at: Department of Mathematics, Tulane University, New Orleans, LA 70118, USA.
E-mail address: jchrispe@tulane.edu (J.C. Chrispell).

0167-2789/$ – see front matter © 2011 Elsevier B.V. All rights reserved.
doi:10.1016/j.physd.2011.03.004

on perturbation theory that is valid in the limit of small deviation from the spherical shape. One important result that comes from this theory is that viscoelastic liquid droplets can undergo free oscillations even when their internal viscosity is high. These oscillations are driven by elasticity and not by surface tension as in the case of Newtonian droplets [18].

Here, we focus upon the development of a 2D Navier–Stokes/Oldroyd-B immersed boundary method and, accordingly, use droplet oscillation as a model problem. We extend the previous Stokes/Oldroyd-B immersed boundary algorithm used to model peristaltic pumping [37] and swimming filaments [38] to one that can capture Reynolds number effects. While other numerical approaches have modeled the shear-induced deformation of viscoelastic drops embedded in a viscoelastic matrix (see, for example, [39,40]), this work presents new simulations of oscillatory dynamics of droplets with bulk viscoelasticity. We validate our method through comparison with linear asymptotics and use it to analyze the effects of the liquid viscosity (Reynolds number) and liquid elasticity (Weissenberg number) on shape oscillations of a viscoelastic droplet suspended in a viscoelastic matrix.

2. The mathematical model

The momentum conservation and conservation of mass equations for the motion of an incompressible fluid flow in a given domain Ω as time, t, evolves are

$$\rho\frac{\mathrm{D}\mathbf{u}}{\mathrm{D}t} = \nabla\cdot\mathbf{T}+\mathbf{f} \quad \text{in } \Omega \tag{2.1}$$
$$\nabla\cdot\mathbf{u} = 0 \quad \text{in } \Omega$$

where $\frac{\mathrm{D}}{\mathrm{D}t}$ denotes the material derivative, and the fluid's velocity is given by $\mathbf{u}$, $\mathbf{T}$ denotes the total stress tensor, ρ is the fluid density, and $\mathbf{f}$ denotes the body force density acting on the fluid. The total stress tensor is composed of a pressure piece and an extra stress

$$\mathbf{T} = -p\mathbf{I}+\boldsymbol{\tau} \tag{2.2}$$

with $\mathbf{I}$ representing a unit tensor. A constitutive equation is needed to define the relationship between the extra stress $\boldsymbol{\tau}$ and the fluid velocity. In the case of Newtonian fluids the constitutive equation is

$$\boldsymbol{\tau} = 2\mu_s\mathbf{d}(\mathbf{u}), \tag{2.3}$$

where μ_s denotes the fluid viscosity, and

$$\mathbf{d}(\mathbf{u}) = \frac{1}{2}\left(\nabla\mathbf{u}+(\nabla\mathbf{u})^T\right)$$

denotes the fluid deformation tensor. Using the Newtonian constitutive relationship (2.3) with (2.1) yields the Navier–Stokes equations. More complex incompressible fluids may be modeled if the extra stress $\boldsymbol{\tau}$ is split into a Newtonian or solvent part and a non-Newtonian or viscoelastic part. In this instance the extra stress is

$$\boldsymbol{\tau} = 2\mu_s\mathbf{d}(\mathbf{u})+\boldsymbol{\sigma}$$

where $\boldsymbol{\sigma}$ represents the viscoelastic contribution to the stress tensor. A viscoelastic constitutive model is used to relate the viscoelastic stress contribution to the fluid velocity. Defining the upper convected time derivative of the viscoelastic contribution to the stress tensor as

$$\boldsymbol{\sigma}^{\nabla} \equiv \frac{\mathrm{D}\boldsymbol{\sigma}}{\mathrm{D}t} - \left(\nabla\mathbf{u}\boldsymbol{\sigma}+\boldsymbol{\sigma}(\nabla\mathbf{u})^T\right)$$

the Oldroyd-B [41,42] constitutive model is

$$r_t\boldsymbol{\sigma}^{\nabla}+\boldsymbol{\sigma} = 2\mu_p\mathbf{d}(\mathbf{u}),$$

where r_t denotes a relaxation time and μ_p denotes the polymer contribution to the zero-shear-rate viscosity. The full Oldroyd-B model for a viscoelastic fluid in dimensional form is

$$\boldsymbol{\sigma}+r_t\boldsymbol{\sigma}^{\nabla}-2\mu_p\mathbf{d}(\mathbf{u}) = \mathbf{0} \quad \text{in } \Omega \tag{2.4}$$

$$\rho\frac{\mathrm{D}\mathbf{u}}{\mathrm{D}t}+\nabla p-\mu_s\Delta\mathbf{u}-\nabla\cdot\boldsymbol{\sigma} = \mathbf{f} \quad \text{in } \Omega \tag{2.5}$$

$$\nabla\cdot\mathbf{u} = 0 \quad \text{in } \Omega. \tag{2.6}$$

In the immersed boundary formulation, the droplet interface acts as a Dirac delta-function layer of force $\mathbf{f}$ in Eq. (2.5):

$$\mathbf{f}(\mathbf{x},t) = \int_{\Gamma}\mathbf{F}(\mathbf{X},t)\delta(\mathbf{x}-\mathbf{X}(\xi,t))\,\mathrm{d}\xi \tag{2.7}$$

where $\mathbf{F}$ is the force density along the interface, the droplet boundary is Γ, and the position of the boundary is described in a Lagrangian frame by $\mathbf{X}(\xi,t)$, with $t\in[0,T]$. For the droplet, $\mathbf{F}$ is proportional to the curvature in the direction of the normal vector

$$\mathbf{F}(\xi) = \sigma_b\kappa(\xi)\mathbf{n}, \tag{2.8}$$

where σ_b is the interfacial tension.

Denoting dimensionless quantities with a prime, a dimensionless Oldroyd-B model is obtained making the change of variables:

$$\boldsymbol{\sigma}' = \frac{L\boldsymbol{\sigma}}{\mu_0 U}, \qquad x' = \frac{x}{L}, \qquad \mathbf{u}' = \frac{\mathbf{u}}{U},$$
$$t' = \frac{tU}{L}, \qquad p' = \frac{Lp}{\mu_0 U}, \qquad \mathbf{f}' = \frac{\mathbf{f}L^2}{\mu_0 U},$$

where L and U are characteristic length and velocity scales respectively, and $\mu_0 = \mu_s+\mu_p$. After substitution, the conservation of momentum, mass, and constitutive equations of the nondimensional Oldroyd-B model may be written as (dropping primes)

$$\boldsymbol{\sigma}+\mathrm{Wi}\,\boldsymbol{\sigma}^{\nabla}-2\alpha\mathbf{d}(\mathbf{u}) = \mathbf{0} \quad \text{in } \Omega \tag{2.9}$$

$$\mathrm{Re}\frac{\mathrm{D}\mathbf{u}}{\mathrm{D}t}+\nabla p-(1-\alpha)\Delta\mathbf{u}-\nabla\cdot\boldsymbol{\sigma} = \mathbf{f} \quad \text{in } \Omega \tag{2.10}$$

$$\nabla\cdot\mathbf{u} = 0 \quad \text{in } \Omega \tag{2.11}$$

where

$$\mathrm{Re} = \frac{LU\rho}{\mu_0}, \qquad \mathrm{Wi} = \frac{r_t U}{L}, \qquad \alpha = \frac{\mu_p}{\mu_0}.$$

Here Wi is fluid Weissenberg number, Re denotes the fluid Reynolds number, and $\alpha\in(0,1)$, denotes the fraction of the total viscosity that is viscoelastic. When simulating Newtonian fluids, the Weissenberg number, Wi , and viscoelastic viscosity fraction, α, are both set to zero. The value of α is $\frac{1}{2}$ in all viscoelastic simulations.

The no-slip condition between the immersed boundary and the fluid is imposed by requiring that it move with the fluid:

$$\mathbf{u}(\mathbf{X}(\xi,t),t) = \frac{\partial\mathbf{X}(\xi,t)}{\partial t} = \int_{\Omega}\mathbf{u}(\mathbf{x},t)\delta(\mathbf{x}-\mathbf{X}(\xi,t))\,\mathrm{d}\mathbf{x}. \tag{2.12}$$

Expressions (2.12) and (2.7) couple the Lagrangian immersed boundary with the Eulerian description of the fluid flow. The closed immersed boundary will be parameterized by an angular variable θ. Note that we will be tracking the dynamics of the boundary due to an initial cosine perturbation of its equilibrium circular configuration. This initial configuration is expressed in the dimensionless form

$$r(\theta) = (R/L)+(A/L)\cos(n\theta). \tag{2.13}$$

For a given radial configuration $r(\theta)$ of the immersed boundary, the nondimensional force density is

$$\mathbf{F}(\theta) = \left(\frac{\sigma_b}{\mu_0 U}\right)\kappa(\theta)\mathbf{n} = \mathrm{Ca}^{-1}\kappa(\theta)\mathbf{n} \tag{2.14}$$

where

$$\kappa(\theta) = \frac{r(\theta)^2+2(r'(\theta))^2-r(\theta)r''(\theta)}{\left[(r(\theta))^2+(r'(\theta))^2\right]^{\frac{3}{2}}}$$

is the dimensionless curvature of the boundary, and we define the capillary number as $\mathrm{Ca} = \mu_0 U/\sigma_b$.

Please cite this article in press as: J.C. Chrispell, et al., Shape oscillations of a droplet in an Oldroyd-B fluid, Physica D (2011), doi:10.1016/j.physd.2011.03.004

3. The numerical method

In order to computationally model the movement of a droplet in an Oldroyd-B fluid, a 2D periodic domain Ω is discretized using a MAC (marker and cell) grid of cell size h. MAC grids store pressure and diagonal stress components at cell centers, the off diagonal component of the viscoelastic contribution to the extra stress $\boldsymbol{\sigma}$ is stored at cell corners, and the x and y components of the fluid's velocity are stored at the centers of vertical and horizontal cell edges respectively [43,37]. With this grid structure defined, the total simulation time T is discretized into N equally spaced time steps with $\Delta t = T/N$. Defining $t^n = n\Delta t$, a fractional step method based on the Navier–Stokes projection scheme presented by Kim and Moin [44] and the Stokes–Oldroyd-B scheme presented by Teran et al. [37] is used to advance the simulation in time. The spatial derivatives are discretized using second-order finite differences. Second-order interpolation is used to define quantities at locations other than the regular corner, center or cell edge.

3.1. Temporal discretization

We introduce an intermediate velocity $\mathbf{u}^*$ and scalar function $\hat{p}$. The solution is advanced from t^n to t^{n+1} by solving an expression for the intermediate velocity $\mathbf{u}^*$, projecting it into a divergence-free space, and then explicitly updating the viscoelastic component of the extra stress. Mathematically each step is described as follows:

Step 1 (*Velocity*): A Crank–Nicolson method and a second-order Adams–Bashforth method are used to construct the intermediate velocity field $\mathbf{u}^*$:

$$\frac{\mathbf{u}^* - \mathbf{u}^n}{\Delta t} = \frac{1}{2}\left(\mathbf{u}^{n-1}\cdot\nabla_h\mathbf{u}^{n-1} - 3\mathbf{u}^n\cdot\nabla_h\mathbf{u}^n\right) + \frac{(1-\alpha)}{2\mathrm{Re}}\Delta_h\left(\mathbf{u}^* + \mathbf{u}^n\right) - \frac{1}{\mathrm{Re}}\nabla_h\cdot\boldsymbol{\sigma}^n + \frac{1}{\mathrm{Re}}\mathbf{f}^n \quad (3.1)$$

where the subscript h on the differential operators refers to a finite difference approximation.

Step 2 (*Projection*): By solving the Poisson problem

$$\Delta_h\hat{p} = \frac{1}{\Delta t}\nabla_h\cdot\mathbf{u}^*, \quad (3.2)$$

a divergence-free velocity can be obtained using

$$\mathbf{u}^{n+1} = \mathbf{u}^* - \Delta t\nabla_h\hat{p}.$$

Step 3 (*Stress*): Writing (2.9) as

$$\frac{\partial\boldsymbol{\sigma}}{\partial t} = \mathbf{g}(\boldsymbol{\sigma},\mathbf{u}), \quad (3.3)$$

where

$$\mathbf{g}(\boldsymbol{\sigma},\mathbf{u}) = \frac{2\alpha}{\mathrm{Wi}}\mathbf{d}(\mathbf{u}) - \frac{1}{\mathrm{Wi}}\boldsymbol{\sigma} - \left(\mathbf{u}\cdot\nabla_h\boldsymbol{\sigma} - (\nabla_h\mathbf{u})\boldsymbol{\sigma} - \boldsymbol{\sigma}(\nabla_h\mathbf{u})^T\right), \quad (3.4)$$

allows $\boldsymbol{\sigma}$ to be explicitly updated. Specifically, we use a second-order Runge–Kutta method to update $\boldsymbol{\sigma}$ by defining two intermediate values of the viscoelastic extra stress $\boldsymbol{\sigma}^{n+A}$ and $\boldsymbol{\sigma}^{n+B}$. With

$$\boldsymbol{\sigma}^{n+A} = \boldsymbol{\sigma}^n + \Delta t\mathbf{g}(\boldsymbol{\sigma}^n,\mathbf{u}^{n+1}), \quad (3.5)$$

$$\boldsymbol{\sigma}^{n+B} = \boldsymbol{\sigma}^{n+A} + \Delta t\,\mathbf{g}(\boldsymbol{\sigma}^{n+A},\mathbf{u}^{n+1}), \quad (3.6)$$

then

$$\boldsymbol{\sigma}^{n+1} = \frac{\boldsymbol{\sigma}^n + \boldsymbol{\sigma}^{n+B}}{2}. \quad (3.7)$$

The linear systems in Steps 1 and 2 are solved using a generalized minimal residual (GMRES) solver. In the absence of an immersed boundary, this algorithm is second order in both space and time for velocity and stress evolution.

The immersed boundary and fluid interaction

The force density function is described in terms of a Dirac delta function in (2.7). As in [45], we choose the discretized delta function $\delta_h(\mathbf{x}) = \phi_h(x)\phi_h(y)$ where h denotes the grid spacing, and

$$\phi_h(r) = \begin{cases} \frac{1}{8h}\left(3 - \frac{2|r|}{h} + \sqrt{1 + \frac{4|r|}{h} - \frac{4r^2}{h^2}}\right) \\ \quad \text{if } |r| \in [0,h], \\ \frac{1}{8h}\left(5 - \frac{2|r|}{h} - \sqrt{-7 + \frac{12|r|}{h} - \frac{4r^2}{h^2}}\right) \\ \quad \text{if } |r| \in [h,2h], \\ 0 \quad \text{otherwise.} \end{cases}$$

The function $\delta_h(\mathbf{x})$ has a support of 16 grid cells. Denoting a Lagrangian point by $\mathbf{X}_k$ and the corresponding Lagrangian force density by $\mathbf{F}_k$, discrete versions of (2.12) and (2.7) are

$$\mathbf{u}_k = \sum_{i,j}\mathbf{u}_{i,j}\delta_h(\mathbf{x}_{i,j} - \mathbf{X}_k)h^2, \quad (3.8)$$

and

$$\mathbf{f}_{i,j} = \sum_k \mathbf{F}_k\delta_h(\mathbf{x}_{i,j} - \mathbf{X}_k)\Delta l_k. \quad (3.9)$$

Here, Δl_k represents the spacing between the discrete immersed boundary points X_k and X_{k+1}.

Immersed droplet forces

Immersed boundary points are initially seeded at equally spaced points along the perturbed droplet interface. To compute the surface tension force supported by this interface, a discrete approximation to (2.14) is calculated using a cubic spline of the immersed boundary points to determine the derivatives of the radial position r' and r'' when calculating the curvature $\kappa(\theta)$. Over the course of a simulation the spacing of the immersed boundary points representing the droplet interface changes. In order to maintain a uniform spacing of the immersed boundary points throughout each simulation, we periodically redistribute the points using cubic splines. This redistribution of points is done every ten time steps in the simulations presented.

A summary of the algorithm

Given the position of the immersed boundary $\mathbf{X}^n$ and values of the stress tensor $\boldsymbol{\sigma}^n$, and velocity $\mathbf{u}^n$ at time $n\Delta t$, the simulation is advanced from time t^n to t^{n+1} by:

- Calculating the force $\mathbf{F}_k$ on the immersed boundary points using cubic splines.
- Spreading the values $\mathbf{F}_k$ using the regularized delta function δ_h to the computational grid with (3.9).
- Solving the Oldroyd-B/Navier–Stokes equations as described in the three steps above.
- Updating the position of the immersed boundary points with the interpolated fluid velocity field via (3.8).
- If necessary, repositioning the immersed boundary points to be equally spaced on the droplet interface using cubic splines.

4. Numerical results

The movement of an immersed droplet in a viscoelastic fluid can be significantly different from that of a droplet in a Newtonian fluid. In this section we show that the addition of a viscoelastic contribution to the extra stress enhances and even generates oscillations in the movement of the immersed boundary.

Please cite this article in press as: J.C. Chrispell, et al., Shape oscillations of a droplet in an Oldroyd-B fluid, Physica D (2011), doi:10.1016/j.physd.2011.03.004

Table 4.1
Case study parameters.

Parameter	Symbol	Value
Domain	Ω	$(-2.5, 2.5) \times (-2.5, 2.5)$
Grid spacing	h	0.01953125
Time step	Δt	0.0008
Base radius	R	1
Perturbation amplitude	A	0.2
Main mode	n	3
Number boundary points	IB_{pts}	698
Capillary number	Ca	0.4

Viscoelastic oscillations

As a base case, the motion of a droplet with the third mode perturbed ($n = 3$) composed of 698 immersed boundary points (IB_{pts}), centered in a square periodic domain, discretized with 256 grid cells in both x and y, such that the droplet has radius $R = 1$, perturbation amplitude $A = 0.2$, and capillary number Ca $= 0.4$, is examined. These base parameters are given in Table 4.1. The geometry of the initial droplet configuration for this base case can be seen in the $t = 0$ frame of Fig. 4.9.

We note that a capillary number of 0.4 is a feature of droplets studied in the physical experiments of Sibillo [46] and the numerical simulation of Afkhami et al. [39]. This value of a capillary number may also be achieved in biological experiments, e.g., for bacteria moving in the cytoplasm of leukocytes or other living cells. Indeed, if we take into account that the cytoplasmic viscosity of human leukocytes is 5 Pa s [15] and their cortical tension (which corresponds to surface tension of liquid droplets) is 30 μN/m [47] and assume that the velocity of leukocytes during their interaction with vascular endothelial cells at low shear stresses (less 0.1 Pa) is 2–4 μm/s [48], then bacteria moving inside these cells will be characterized by a capillary number between 0.33 and 0.67.

As n-mode cosine perturbations of a circle are used for the initial droplet configuration (2.13), the time dependent movement of the droplet may be described by tracking the amplitude of the nth Fourier coefficient, $C_n(t)$. We acknowledge that nonlinearities may excite other modes, but here we focus on the dominant mode. For the base case (listed in Table 4.1) tracking the $n = 3$ mode Fourier coefficient, $C_3(t)$, reveals the droplet motion. The value for C_3 at each recorded time step is calculated by equally distributing 512 points (in arc length) on a cubic spline of the immersed boundary points, then scaling their three-mode Fourier transform coefficient by $1/(256A)$ to insure that $C_3(0) = 1$.

The evolution of $C_3(t)$ for a Newtonian droplet using the parameters in Table 4.1 at different values of the Reynolds number are shown in Fig. 4.1. As expected from previous studies [9,18], a decrease in the Reynolds number eventually leads to an aperiodic decay of a perturbed droplet. In our case, the sinusoidal oscillations in the tracked Fourier mode, C_3, appear to be nonexistent for Re $=$ 1.

The effects of viscoelasticity on the movement of the droplet become evident upon looking at the tracked Fourier mode for simulations using the parameters in Table 4.1, fixing Re $= 1$, and increasing the value of the Weissenberg number (see Fig. 4.2). In this low Reynolds number case it is observed that as the Weissenberg number is increased, the droplet shows sinusoidal oscillations that were not present in the Newtonian simulation.

To further investigate the effects of viscoelasticity on the immersed boundary's movement we consider a fluid with Re $=$ 10 and the base parameters from Table 4.1. The computed value of C_3 is shown in Fig. 4.3 for fluids with Weissenberg numbers Wi $= 0, 0.1$, and 0.7. It can be seen that the droplet boundary oscillates with a frequency and decay rate that are dependent on the Weissenberg number. Fig. 4.4 examines the values of the C_6 Fourier transform coefficient for simulations with Wi $= 0, 0.1,$ and 0.7, scaled by $1/(256A^2)$. It can be seen from Figs. 4.3 and 4.4 that the dominant mode in each simulation is represented by the C_3 Fourier coefficient.

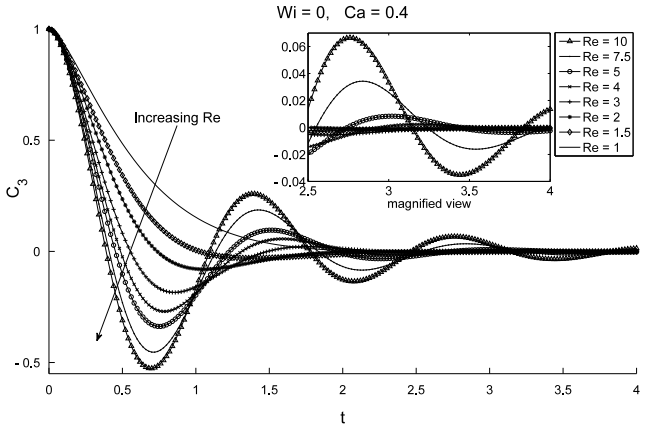

Fig. 4.1. Tracked Fourier coefficient, C_3, versus t for Newtonian fluids of varying Reynolds number.

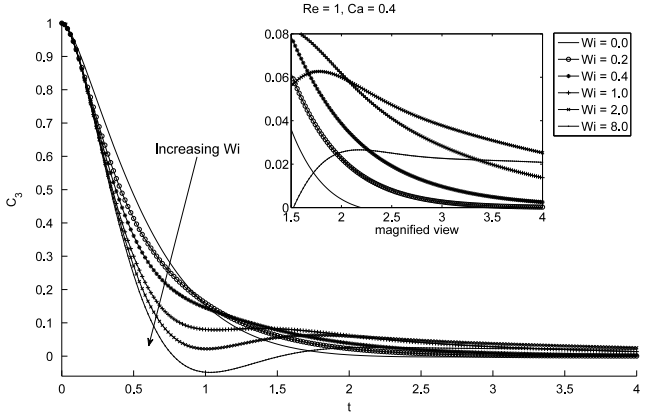

Fig. 4.2. Tracked Fourier coefficient, C_3, versus t for fluids with Re $= 1$ and varying Weissenberg number Wi .

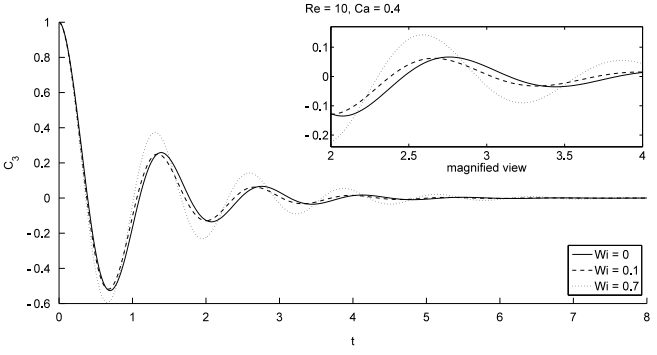

Fig. 4.3. Three-mode Fourier coefficient for Wi $= 0, 0.1,$ and 0.7.

In order to quantify the decay rate, d_r, and oscillation frequency, ω, that provide a description of the droplet movement, the Fourier mode C_3 is approximated by

$$C_3(t) \approx e^{(-d_r t)} \left(\cos(\omega t) + c \sin(\omega t)\right). \tag{4.1}$$

Using a nonlinear least squares algorithm, parameters d_r, ω, and c are found that best fit the numerical data. Fig. 4.5 shows a comparison between the best fit approximation to $C_3(t)$ described by setting d_r, ω, and c to 0.7211, 4.8307, and 0.1801 in (4.1) respectively, for a simulation with Re $= 10$, Wi $= 1.0$ and the base case parameters stated in Table 4.1.

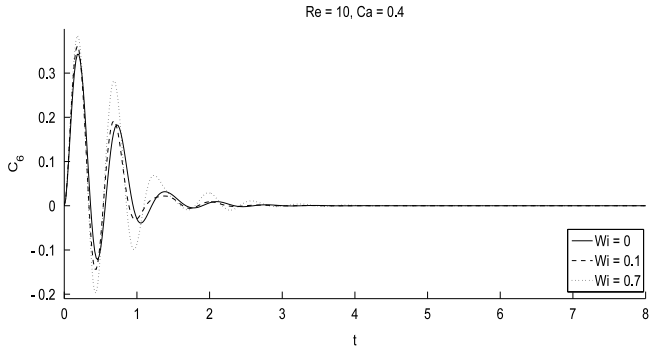

Fig. 4.4. Six-mode Fourier coefficient for Wi = 0, 0.1, and 0.7.

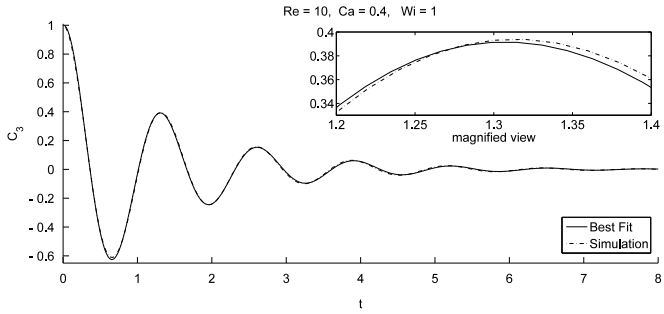

Fig. 4.5. Plot of the C_3 Fourier coefficient versus time and the best fit function using a nonlinear least squares routine.

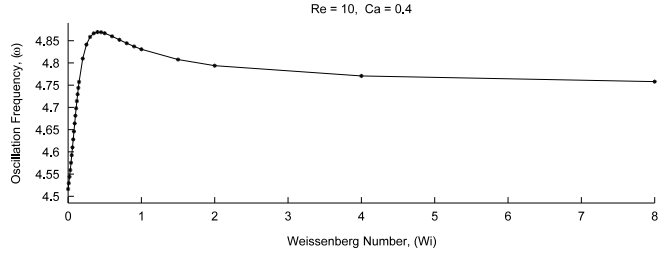

Fig. 4.6. Oscillation frequency versus Weissenberg number for Re = 10 fluid with capillary number Ca = 0.4.

Using the nonlinear least square fit gives a method of classifying the droplet movement and allows for the effects of viscoelasticity to be examined as a function of the Weissenberg number, Wi. Figs. 4.6 and 4.7 show computed decay rates and oscillation frequencies as a function of the Weissenberg number for the base case with Re = 10. Note that there is a sharp increase in oscillation frequency as the fluid moves from the Newtonian to the viscoelastic case, reaches a maximum somewhere short of Wi = 1 and then saturates to a steady value. Moreover, for small Weissenberg numbers, droplet oscillations are damped more quickly than in the Newtonian case; however, after a critical value of the Weissenberg number the decay rate of the oscillations drops below that of the Newtonian case and approaches an asymptotic limit. Thus, for viscoelastic fluids with high values of the Weissenberg number, oscillations last longer than in Newtonian fluids.

4.1. Stress plots

The trace of the stress tensor $\boldsymbol{\sigma}$ measures the mean square distension of the microscopic polymer coils in the Oldroyd-B model of a viscoelastic fluid. Fig. 4.8 shows the contours of $\mathrm{tr}(\boldsymbol{\sigma})$ for a droplet simulation with Re = 10, Wi = 1, and other parameters set as in Table 4.1. Throughout the simulation the $\mathrm{tr}(\boldsymbol{\sigma})$ swells and

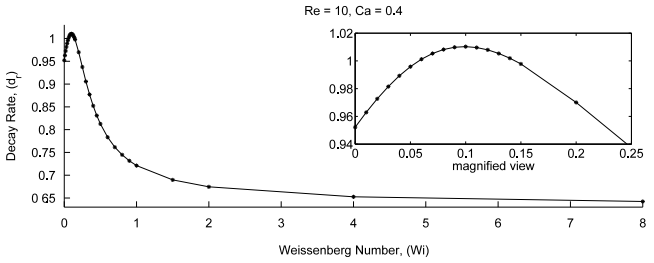

Fig. 4.7. Decay rate versus Weissenberg number for Re = 10 fluid with capillary number Ca = 0.4.

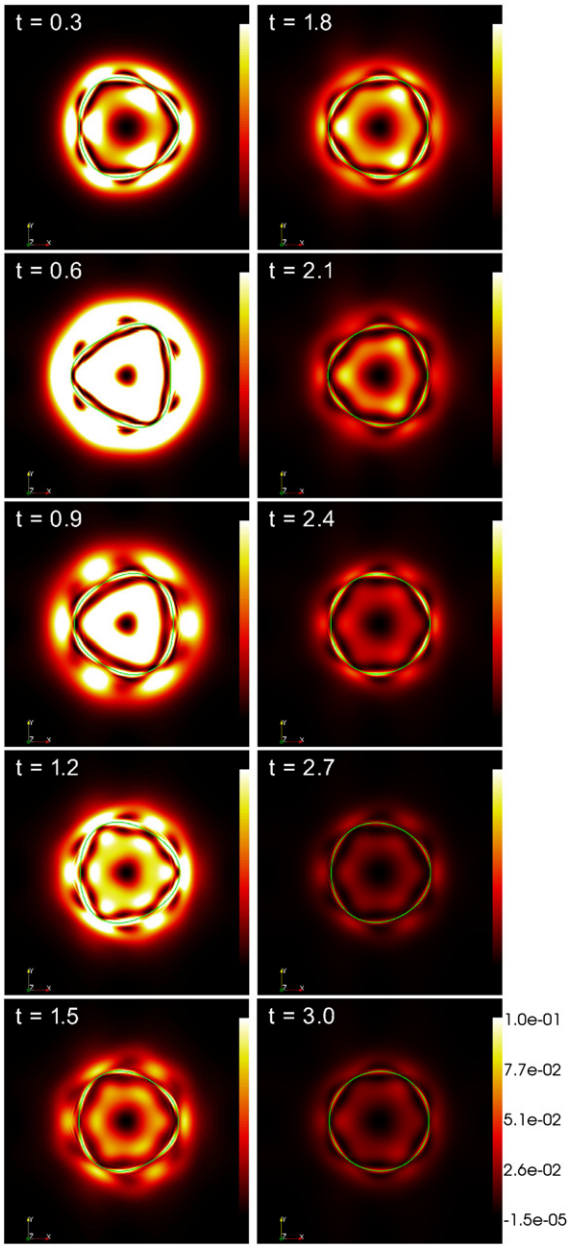

Fig. 4.8. Plot showing the magnitude of the trace of the viscoelastic extra stress, $\boldsymbol{\sigma}$, at varying times throughout a simulation with Re = 10, and Wi = 1.

drops in the region directly surrounding and inside the droplet, and the simulation shows polymer distension in the fluid even after the droplet interface appears visually to have stopped moving.

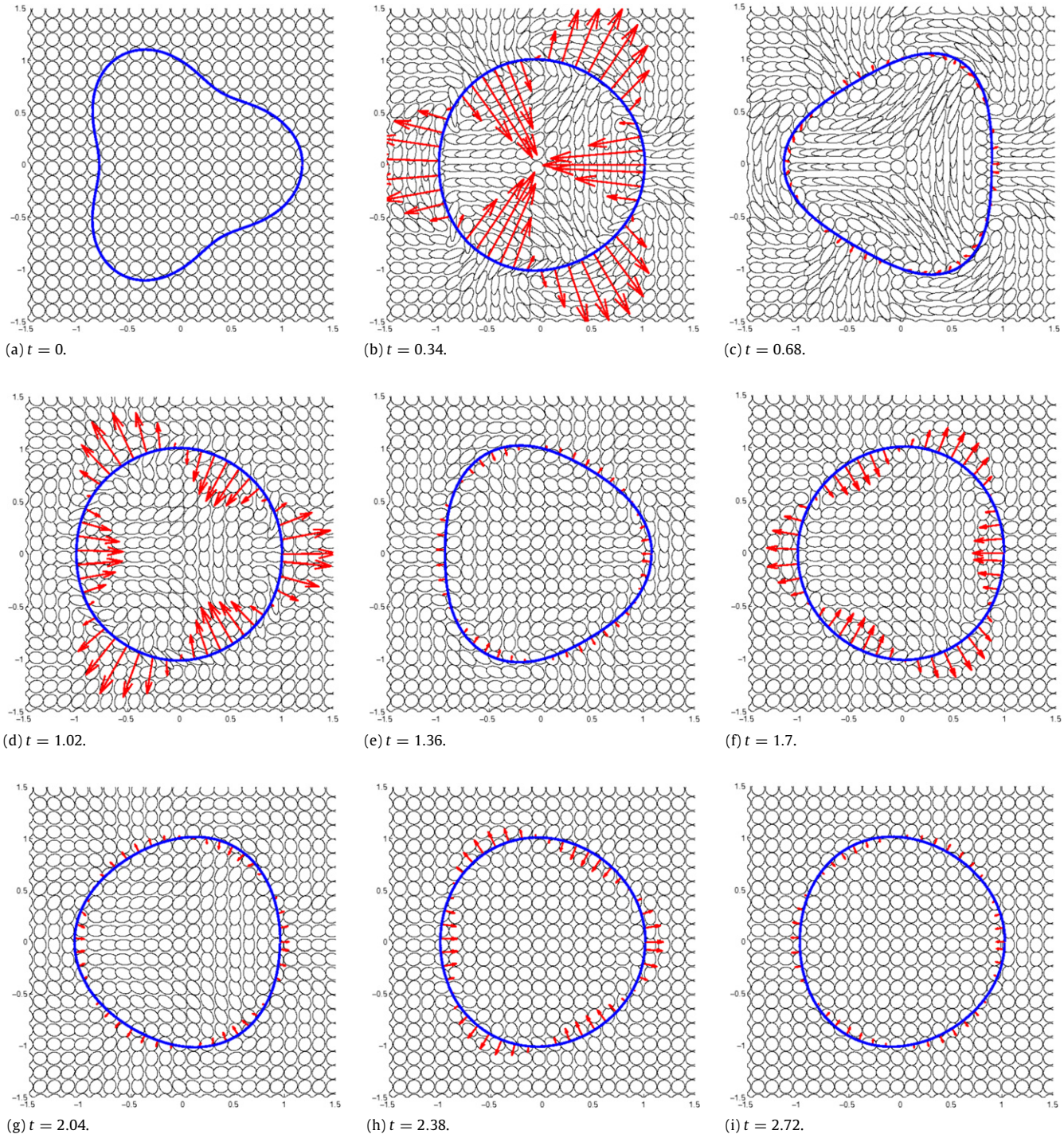

(a) $t = 0$. (b) $t = 0.34$. (c) $t = 0.68$.

(d) $t = 1.02$. (e) $t = 1.36$. (f) $t = 1.7$.

(g) $t = 2.04$. (h) $t = 2.38$. (i) $t = 2.72$.

Fig. 4.9. Stress ellipses based on $\hat{\boldsymbol{\sigma}}$ for a fluid with Re $= 10$ and Wi $= 1$ indicate that polymer coils are stretched in the region near the interface, but slowly relax, as these ellipses return to their circular shape. Velocity vectors have been placed on the immersed boundary to indicate the droplet's current motion.

As in [38], we consider the polymer stress tensor at a point under the following shift:

$$\hat{\boldsymbol{\sigma}} = \frac{\text{Wi}}{\alpha}\boldsymbol{\sigma} + \mathbf{I}. \tag{4.2}$$

This shifted stress tensor, $\hat{\boldsymbol{\sigma}}$, results from an alternate nondimensionalization of the Navier–Stokes/Oldroyd-B system using the change of variables

$$\hat{\boldsymbol{\sigma}}' = \frac{r_t\boldsymbol{\sigma}}{\mu_p} + \mathbf{I}, \qquad x' = \frac{x}{L}, \qquad \mathbf{u}' = \frac{\mathbf{u}}{U},$$

$$t' = \frac{tU}{L}, \qquad p' = \frac{Lp}{\mu_s U}, \qquad \mathbf{f}' = \frac{\mathbf{f}L^2}{\mu_s U}.$$

The tensor $\hat{\boldsymbol{\sigma}}$ has two positive eigenvalues, e_1 and e_2, and corresponding orthogonal eigenvectors, d_1 and d_2. The eigenvector corresponding to the maximal eigenvalue indicates the direction of the maximal distension of the polymer field, and the eigenvalue indicates the degree of distension. Using the eigenvalues to scale the length of the axes of an ellipse aligned with the eigenvectors, and centered at the given point, gives a technique for visualizing the polymer distension in the fluid. Stress tensor $\hat{\boldsymbol{\sigma}}$ represents an initial zero-stress field $\boldsymbol{\sigma} = \mathbf{0}$ by circles of radius 1.

Please cite this article in press as: J.C. Chrispell, et al., Shape oscillations of a droplet in an Oldroyd-B fluid, Physica D (2011), doi:10.1016/j.physd.2011.03.004

Fig. 4.9 shows a sequence of frames depicting the position of the droplet interface and the stess-ellipse field from a simulation using the base case parameters (Table 4.1), with Weissenberg number Wi = 1 and Re = 10.0. Velocity vectors plotted on the droplet interface show that as the droplet oscillates, the polymer coils are stretched in the region near the interface, and then slowly relax, as indicated by the ellipses returning to a circular shape as the droplet approaches its equilibrium.

5. Linear analysis

In order to validate our viscoelastic immersed boundary implementation, a comparison with linear asymptotics is considered. In [49], the analysis of a closed elastic membrane in two-dimensional Navier–Stokes flow was presented in the context of resonances due to a periodic driving force. The linearized Oldroyd-B equations can be written in a way that fits the same linear analysis as follows. Linearizing the model equations leads to

$$\boldsymbol{\sigma} + \mathrm{Wi}\,\frac{\partial \boldsymbol{\sigma}}{\partial t} - 2\alpha \mathbf{d}(\mathbf{u}) = \mathbf{0} \tag{5.1}$$

$$\mathrm{Re}\left(\frac{\partial \mathbf{u}}{\partial t}\right) + \nabla p - (1-\alpha)\Delta \mathbf{u} - \nabla \cdot \boldsymbol{\sigma} = \mathbf{f}. \tag{5.2}$$

Since the resulting motion of the droplet is oscillatory, one can introduce the time dependence of all variables explicitly to be of the form $\exp(\mathrm{i}\gamma t)$, where the real and imaginary parts of γ provide the oscillation frequency and damping, respectively. Substituting $\partial\boldsymbol{\sigma}/\partial t = \mathrm{i}\gamma\,\boldsymbol{\sigma}$ into Eq. (5.1) (and similarly for other variables) gives

$$(1 + \mathrm{Wi}\,\gamma \mathrm{i})\boldsymbol{\sigma} = 2\alpha \mathbf{d}(\mathbf{u}) \Rightarrow \boldsymbol{\sigma} = \frac{2\alpha}{(1+\mathrm{Wi}\,\gamma \mathrm{i})}\mathbf{d}(\mathbf{u})$$

and plugging this into Eq. (5.2) leads to

$$\mathrm{Re}\gamma \mathrm{i}\mathbf{u} + \nabla p - (1-\alpha)\Delta \mathbf{u} - \frac{2\alpha}{(1+\mathrm{Wi}\,\gamma \mathrm{i})}\nabla \cdot \mathbf{d}(\mathbf{u}) = \mathbf{f}.$$

Using the identity $2\nabla \cdot \mathbf{d}(\mathbf{u}) = \Delta \mathbf{u}$ we get

$$\mathrm{Re}\gamma \mathrm{i}\mathbf{u} + \nabla p - \frac{1 + \mathrm{Wi}\,\gamma \mathrm{i}(1-\alpha)}{(1+\mathrm{Wi}\,\gamma \mathrm{i})}\Delta \mathbf{u} = \mathbf{f}$$

which we can write as

$$\gamma \mathrm{i}\mathbf{u} + \nabla \hat{p} - \frac{1}{R_{\mathrm{Wi}}}\Delta \mathbf{u} = \hat{\mathbf{f}} \tag{5.3}$$

where $\mathrm{Re}\,\hat{p} = p$, $\mathrm{Re}\,\hat{\mathbf{f}} = \mathbf{f}$ and $R_{\mathrm{Wi}} = \frac{1+\mathrm{Wi}\,\gamma \mathrm{i}}{1+\mathrm{Wi}\,\gamma \mathrm{i}(1-\alpha)}\mathrm{Re}$. Eq. (5.3) was analyzed in [49] in the context of a closed elastic membrane in a two-dimensional Newtonian fluid, where Wi = 0. Here we modify that analysis to account for the viscoelastic effects.

A circular interface is given an n-mode perturbation of small amplitude A and all variables are expanded in powers of A. The spatial dependence of the droplet interface is written in polar coordinates as $\mathbf{X}(r,\theta) = \mathrm{e}^{\mathrm{i}\theta}(X^r(r), X^\theta(r))$ and the corresponding equations for the radial functions are derived to leading order with appropriate jump conditions across the interface. Enforcing the jump conditions results in a linear system for the leading-order interface location as

$$\mathcal{M}\begin{pmatrix} X^r \\ X^\theta \end{pmatrix} = \begin{pmatrix} 0 \\ 0 \end{pmatrix}.$$

In order to obtain a nontrivial solution, the determinant of $\mathcal{M}$ must equal zero, leading to a dispersion relation in the implicit form

$$\mathcal{D}(n, \gamma, R_{\mathrm{Wi}}) = 0$$

for given capillary number, Ca. It is difficult to get an explicit relationship between γ and n in general since the dispersion relation involves ratios of Hankel functions whose arguments depend on γ and R_{Wi}, which was a fixed parameter in [49]. We derived an expansion for γ in terms of R_{Wi} and substituted it into the definition of R_{Wi} in Eq. (5.3). This leads to a Padé approximation for γ:

$$\mathrm{i}\gamma = -d_r + \mathrm{i}\omega \approx \frac{\sum_{k=0}^{m} a_k(\mathrm{Wi})\epsilon^k}{\sum_{k=0}^{m} b_k(\mathrm{Wi})\epsilon^k} \tag{5.4}$$

where $\epsilon = \mathrm{Re}^{-1/2}$. We verified numerically that the approximation is valid for moderate to high values of Re with $m = 6$.

Since the above analytic expressions for oscillation frequency and damping were derived in the linear regime, we compare them with the fully nonlinear computations for a given small amplitude perturbation $A = 0.02$. Plots comparing the decay rate and oscillation frequency computed with our method to the asymptotic values in Eq. (5.4) are given in Figs. 5.1–5.4 for fluids with Re = 10 and Re = 100, and Ca = 1.

Figs. 5.1 and 5.2 show that the immersed boundary calculations of decay rate and oscillation frequency follow very closely the pattern predicted by the linear theory for a fluid with Re = 10. Figs. 5.3 and 5.4 indicate that the oscillation frequency and decay rates obtained via simulation are converging toward values near those predicted by the linear theory. Assuming that the computed oscillation frequency, ω_h, converges monotonically to the true value ω, a value for the convergence rate (Cvge. Rate) may be computed using the expression

$$\text{Cvge. Rate} = \left(\frac{-1}{\ln(2)}\right)\ln\left(\frac{\|\omega_{h_2}\| - \|\omega_{h_3}\|}{\|\omega_{h_1}\| - \|\omega_{h_2}\|}\right), \tag{5.5}$$

where the grid spacings are such that $h_1 = 2h_2 = 4h_3$. Table 5.2 confirms the convergence of both the oscillation frequency and the decay rate for simulations done with Weissenberg number Wi = 8 when Re = 100.

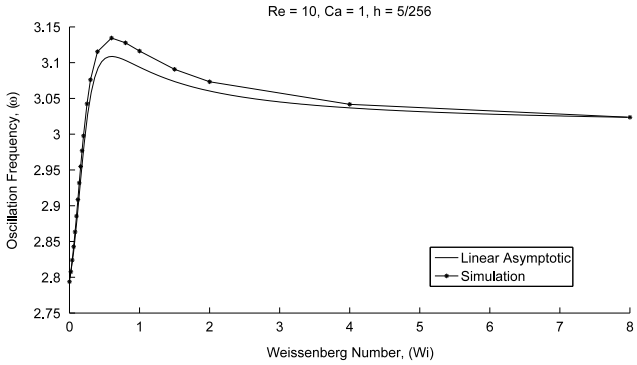

Fig. 5.1. Re = 10 oscillation frequency.

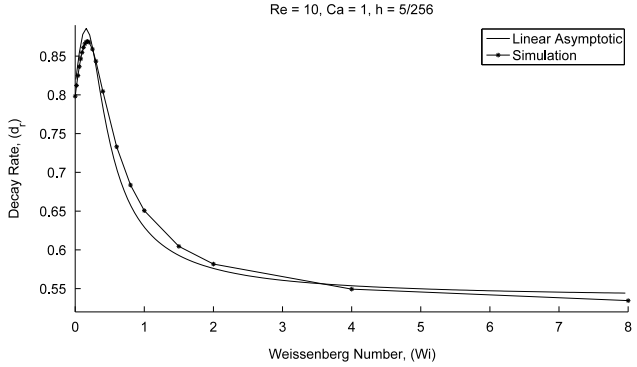

Fig. 5.2. Re = 10 decay rate.

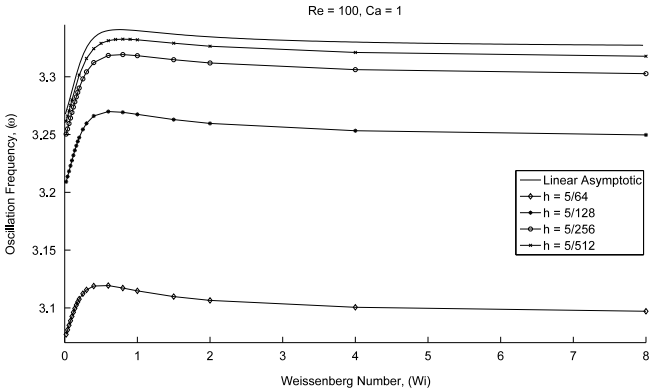

Fig. 5.3. Re = 100 oscillation frequency.

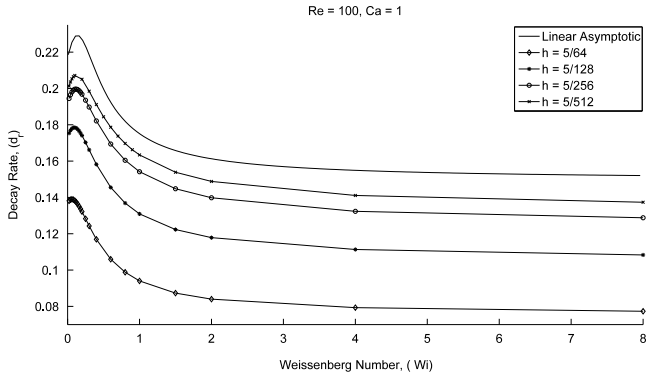

Fig. 5.4. Re = 100 decay rate.

Table 5.2
Convergence rates found for ω and d_r with Re = 100 and Wi = 8.

Grid: $(\Delta t, h)$	$\left(\frac{2.5}{2500}, \frac{5}{64}\right)$	$\left(\frac{2.5}{5000}, \frac{5}{128}\right)$	$\left(\frac{2.5}{10\,000}, \frac{5}{265}\right)$	$\left(\frac{2.5}{20\,000}, \frac{5}{512}\right)$
ω	3.0971	3.2497	3.3027	3.3177
Cvge. Rate	–	–	1.52	1.81
d_r	0.0773	0.1083	0.1288	0.1374
Cvge. Rate	–	–	0.60	1.26

6. Conclusions

We have developed a two-dimensional Navier–Stokes immersed boundary algorithm for the flow of immiscible viscoelastic (Oldroyd-B) liquids. Using this algorithm, we studied the effect of bulk viscoelasticity on free shape oscillations of a liquid droplet at different Reynolds numbers. In the case of a moderate to high Reynolds number, our numerical simulations show that viscoelasticity causes an increase in oscillation frequency and, at Weissenberg number above the critical value, a decrease in the decay rate of droplet oscillations. When the Reynolds number falls below the critical value for shape oscillations of a Newtonian droplet, our model predicts reappearance of the oscillations when viscoelasticity is introduced. Both of these results agree well with previous asymptotic analysis of viscoelastic drop oscillations [18]. In addition to this supporting evidence, the numerical method was validated by direct comparison of the decay rates and oscillation frequencies predicted by the linear theory to those computed numerically. A natural extension of this algorithm will be one in which the fluid interior to the droplet has different viscoelastic properties from the fluid exterior to the droplet.

Acknowledgements

The work by J. Chrispell, R. Cortez and L. Fauci was supported in part by NSF DMS 0652775. The work by D. Khismatullin was supported in part by Louisiana Board of Regents grant LEQSF(2007-12)-ENH-PKSFI-PRS-01. We are grateful to Douglas Varela for insightful conversations.

References

[1] G.I. Taylor, The formation of emulsion in definable field of flow, Proc. R. Soc. A 146 (1934) 501–523.
[2] A. Nadim, A concise introduction to surface rheology with application to dilute emulsions of viscous drops, Chem. Eng. Commun. 148 (1) (1996) 391–407.
[3] J.G. McDaniel, I. Akhatov, R.G. Holt, Inviscid dynamics of a wet foam drop with monodisperse bubble size distribution, Phys. Fluids 14 (2002) 1886–1894.
[4] A.I. Grigorév, A.R. Gaibov, On acoustic radiation accompanying vibrations of a charged droplet, Tech. Phys. 46 (11) (2001) 1351–1357.
[5] R. Shaw, Particle–turbulence interactions in atmospheric clouds, Annu. Rev. Fluid Mech. 35 (2003) 183–227.
[6] Z. Zhao, D. Poulikakos, J. Fukai, Heat transfer and fluid dynamics during the collision of a liquid droplet on a substrate—I. modeling, Int. J. Heat Mass Transfer 39 (1996) 2771–2789.
[7] M. Pasandideh-Fard, S. Chandra, J. Mostaghimi, A three-dimensional model of droplet impact and solidification, Int. J. Heat Mass Transfer 45 (2002) 2229–2242.
[8] Lord Rayleigh, On the capillary phenomena of jets, Proc. R. Soc. Lond. 29 (1879) 71–97.
[9] S. Chandrasekhar, Hydrodynamic and Hydromagnetic Stability, Dover, New York, 1961.
[10] R.H. Durisen, R.A. Gingold, J.E. Tohline, A.P. Boss, Dynamic fission instabilities in rapidly rotating $n = 3/2$ polytropes—a comparison of results from finite-difference and smoothed particle hydrodynamics codes, Astrophys. J. 305 (1986) 281–308.
[11] N. Bohr, Disintegration of heavy nuclei, Nature 143 (1939) 330.
[12] S.B. Patel, Nuclear Physics: An Introduction, Wiley, New Delhi, 1991.
[13] E. Evans, A. Yeung, Apparent viscosity and cortical tension of blood granulocytes determined by micropipet aspiration, Biophys. J. 56 (1) (1989) 151–160.
[14] D.B. Khismatullin, G.A. Truskey, Three-dimensional numerical simulation of receptor-mediated leukocyte adhesion to surfaces: effects of cell deformability and viscoelasticity, Phys. Fluids 17 (2005) 031505.
[15] D.B. Khismatullin, The cytoskeleton and deformability of white blood cells, in: Leukocyte Adhesion: Current Topics in Membranes, vol. 64, Elsevier, Academic Press, Amsterdam, 2009, pp. 47–111.
[16] H. Lamb, Hydrodynamics, Dover, New York, 1945.
[17] C.A. Miller, L.E. Scriven, The oscillations of a fluid droplet immersed in another fluid, J. Fluid Mech. 32 (3) (1968) 417–435.
[18] D.B. Khismatullin, A. Nadim, Shape oscillations of a viscoelastic drop, Phys. Rev. E 63 (2001) 061508.
[19] B.M. Rush, A. Nadim, The shape oscillations of a two-dimensional drop including viscous effects, Eng. Anal. Bound. Elem. 24 (2000) 43–51.
[20] T. Shi, R.E. Apfel, Oscillations of a deformed liquid drop in an acoustic field, Phys. Fluids 7 (1995) 1545–1552.
[21] Z.C. Feng, Y.H. Su, Numerical simulations of the translational and shape oscillations of a liquid drop in an acoustic field, Phys. Fluids 9 (1997) 519–529.
[22] O.A. Basaran, Nonlinear oscillations of viscous liquid drops, J. Fluid Mech. 241 (1992) 169–198.
[23] Z. Wang, A.Y. Tong, A sharp surface tension modeling method for two-phase incompressible interfacial flows, Internat. J. Numer. Methods Fluids (2009).
[24] B. Griffith, C. Peskin, On the order of accuracy of the immersed boundary method: higher order convergence rates for sufficiently smooth problems, J. Comput. Phys. 208 (2005) 75–105.
[25] C. Tu, C. Peskin, Stability and instability in the computation of flows with moving immersed boundaries: a comparison of three methods, SIAM J. Sci. Stat. Comput. 13 (6) (1992) 1361–1376.
[26] Y. Mori, C.S. Peskin, Implicit second-order immersed boundary methods with boundary mass, Comput. Methods Appl. Mech. Eng. 197 (25–28) (2008) 2049–2067. Immersed Boundary Method and Its Extensions.
[27] J.M. Stockie, Modelling and simulation of porous immersed boundaries, Comput. Struct. 87 (11–12) (2009) 701–709. Fifth MIT Conference on Computational Fluid and Solid Mechanics.
[28] J.G. McDaniel, R.G. Holt, Measurement of aqueous foam rheology by acoustic levitation, Phys. Rev. E 61 (3) (2000) R2204–R2207.
[29] X. Chen, T. Shi, Y. Tian, J. Jankovsky, R.G. Holt, R.E. Apfel, Numerical simulation of superoscillations of a triton-bearing drop in microgravity, J. Fluid Mech. 367 (1998) 205–220.
[30] Y. Tian, R.G. Holt, R.E. Apfel, Investigation of liquid surface rheology of surfactant solutions by droplet shape oscillations: experiments, J. Colloid Interface Sci. 187 (1997) 1–10.
[31] R.E. Apfel, Y. Tian, J. Jankovsky, T. Shi, X. Chen, R.G. Holt, E. Trinh, A. Croonquist, K.C. Thornton, A. Sacco, C. Coleman, F.W. Leslie, D.H. Matthiesen, Free oscillations and surfactant studies of superdeformed drops in microgravity, Phys. Rev. Lett. 78 (10) (1997) 1912–1915.
[32] P. Erni, P. Fischer, E.J. Windhab, Deformation of single emulsion drops covered with a viscoelastic adsorbed protein layer in simple shear flow, Appl. Phys. Lett. 87 (2005) 244104.
[33] D.M. Sztukowski, H.W. Yarranton, Rheology of asphaltene–toluene/water interfaces, Langmuir 21 (25) (2005) 11651–11658.

[34] E.M. Freer, H. Wong, C.J. Radke, Oscillating drop/bubble tensiometry: effect of viscous forces on the measurement of interfacial tension, J. Colloid Interface Sci. 282 (1) (2005) 128–132.
[35] R. Georgescu, D. Khismatullin, R.G. Holt, J.L. Castagner, O. Aámar, I.J. Bigio, Design of a system to measure light scattering from individual cells excited by an acoustic wave, Opt. Express 16 (6) (2008) 3496–3503.
[36] G. Loglio, P. Pandolfini, R. Miller, F. Ravera, Optical observation of high-frequency drop oscillations by a spectrum compression technique applied to the capillary pressure tensiometry, Langmuir 25 (21) (2009) 12780–12786.
[37] J. Teran, L. Fauci, M. Shelley, Peristaltic pumping and irreversibility of a stokesian viscoelastic fluid, Phys. Fluids 20 (7) (2008) 073101.
[38] J. Teran, L. Fauci, M. Shelley, Viscoelastic fluid response can increase the speed and efficiency of a free swimmer, Phys. Rev. Lett. 104 (2010) 038101.
[39] S. Afkhami, P. Yue, Y. Renardy, A comparison of viscoelastic stress wakes for two-dimensional and three-dimensional Newtonian drop deformations in a viscoelastic matrix under shear, Phys. Fluids 21 (7) (2009) 072106.
[40] P. Yue, J. Feng, C. Lin, J. Shen, Viscoelastic effects on drop deformation in steady shear, J. Fluid Mech. 540 (2005) 427–437.
[41] R.B. Bird, R.C. Armstrong, O. Hassager, Dynamics of Polymeric Liquids, Wiley-Interscience, 1987.
[42] R. Larson, The Structure and Rheology of Complex Fluids, Oxford University Press, Oxford, 1998.
[43] F.H. Harlow, J.E. Welch, Numerical calculation of time-dependent viscous incompressible flow of fluid with free surface, Phys. Fluids 8 (12) (1965) 2182–2189.
[44] J. Kim, P. Moin, Application of a fractional-step method to incompressible Navier–Stokes equations, J. Comput. Phys. 59 (2) (1985) 308–323.
[45] Charles S. Peskin, The immersed boundary method, Acta Numer. 11 (2002) 479–517.
[46] V. Sibillo, M. Simeone, S. Guido, Break-up of a Newtonian drop in a viscoelastic matrix under simple shear flow, Rheol. Acta 43 (2004) 449–456. doi:10.1007/s00397-004-0374-7.
[47] M.A. Tsai, R.S. Frank, R.E. Waugh, Passive mechanical behavior of human neutrophils: power-law fluid, Biophys. J. 65 (5) (1993) 2078–2088.
[48] T. Yago, A. Leppänen, H. Qiu, W.D. Marcus, M.U. Nollert, C. Zhu, R.D. Cummings, R.P. McEver, Distinct molecular and cellular contributions to stabilizing selectin-mediated rolling under flow, J. Cell Biol. 158 (4) (2002) 787–799.
[49] R. Cortez, C.S. Peskin, J.M. Stockie, D. Varela, Parametric resonance in immersed elastic boundaries, SIAM J. Appl. Math. 65 (2) (2004) 494–520.

Please cite this article in press as: J.C. Chrispell, et al., Shape oscillations of a droplet in an Oldroyd-B fluid, Physica D (2011), doi:10.1016/j.physd.2011.03.004